

## The TRMM Multisatellite Precipitation Analysis (TMPA): Quasi-Global, Multiyear, Combined-Sensor Precipitation Estimates at Fine Scales

GEORGE J. HUFFMAN,<sup>\*,+</sup> ROBERT F. ADLER,<sup>\*</sup> DAVID T. BOLVIN,<sup>\*,+</sup> GUOJUN GU,<sup>\*,#</sup> ERIC J. NELKIN,<sup>\*,+</sup>  
KENNETH P. BOWMAN,<sup>@</sup> YANG HONG,<sup>\*,#</sup> ERICH F. STOCKER,<sup>&</sup> AND DAVID B. WOLFF<sup>\*,+</sup>

<sup>\*</sup>Laboratory for Atmospheres, NASA GSFC, Greenbelt, Maryland

<sup>+</sup>Science Systems and Applications, Inc., Lanham, Maryland

<sup>#</sup>Goddard Earth Sciences and Technology Center, University of Maryland, Baltimore County, Baltimore, Maryland

<sup>@</sup>Texas A&M University, College Station, Texas

<sup>&</sup>Global Change Data Center, NASA GSFC, Greenbelt, Maryland

(Manuscript received 8 March 2006, in final form 22 June 2006)

### ABSTRACT

The Tropical Rainfall Measuring Mission (TRMM) Multisatellite Precipitation Analysis (TMPA) provides a calibration-based sequential scheme for combining precipitation estimates from multiple satellites, as well as gauge analyses where feasible, at fine scales ( $0.25^\circ \times 0.25^\circ$  and 3 hourly). TMPA is available both after and in real time, based on calibration by the TRMM Combined Instrument and TRMM Microwave Imager precipitation products, respectively. Only the after-real-time product incorporates gauge data at the present. The dataset covers the latitude band  $50^\circ\text{N}$ – $50^\circ\text{S}$  for the period from 1998 to the delayed present. Early validation results are as follows: the TMPA provides reasonable performance at monthly scales, although it is shown to have precipitation rate–dependent low bias due to lack of sensitivity to low precipitation rates over ocean in one of the input products [based on Advanced Microwave Sounding Unit-B (AMSU-B)]. At finer scales the TMPA is successful at approximately reproducing the surface observation–based histogram of precipitation, as well as reasonably detecting large daily events. The TMPA, however, has lower skill in correctly specifying moderate and light event amounts on short time intervals, in common with other finescale estimators. Examples are provided of a flood event and diurnal cycle determination.

### 1. Introduction

Precipitation displays small-scale variability and highly nonnormal statistical behavior that requires frequent, closely spaced observations for adequate representation. Such observations are not possible through surface-based measurements over much of the globe, particularly in oceanic, remote, or developing regions. Consequently, researchers have come to depend on suites of sensors flying on a variety of satellites over the last 25+ years for the majority of the information used to estimate precipitation on a global basis. While it is possible to create such estimates solely from one type of sensor, researchers have increasingly moved to using combinations of sensors in an attempt to improve accuracy, coverage, and resolution. The first such combi-

nations were performed at a relatively coarse scale to ensure reasonable error characteristics. For example, the Global Precipitation Climatology Project (GPCP) satellite–gauge (SG) combination is computed on a monthly  $2.5^\circ \times 2.5^\circ$  latitude–longitude grid (Huffman et al. 1997; Adler et al. 2003). Subsequently, the scientific community requested that the estimates be made available at finer scale, even at the cost of higher uncertainties. Finer-scale products initiated by the GPCP include the Pentad (Xie et al. 2003) and One-Degree Daily (Huffman et al. 2001) combination estimates of precipitation. Other research groups have introduced a number of finescale estimates in the past several years that are now in quasi-operational production (see Huffman 2005), including the Climate Prediction Center (CFC) morphing algorithm (CMORPH; Joyce et al. 2004), the Naval Research Laboratory Global Blended-Statistical Precipitation Analysis (NRLgeo; Turk and Miller 2005), the Passive Microwave-Calibrated Infrared algorithm (PMIR; Kidd et al. 2003), and the Precipitation Estimation from Remotely Sensed Informa-

---

Corresponding author address: George J. Huffman, NASA GSFC, Code 613.1, Greenbelt, MD 20771.  
E-mail: huffman@agnes.gsfc.nasa.gov

tion Using Artificial Neural Networks (PERSIANN; Sorooshian et al. 2000).

This paper describes the Tropical Rainfall Measuring Mission (TRMM) Multisatellite Precipitation Analysis (TMPA), a new dataset that continues the trend toward routine computation and distribution of finer-scale precipitation estimates. The primary merged microwave-infrared product is computed at the 3-hourly,  $0.25^\circ \times 0.25^\circ$  latitude–longitude resolution. In common with the GPCP products, the TMPA is designed to combine precipitation estimates from various satellite systems, as well as land surface precipitation gauge analyses when possible, with the goal that the final product will have a calibration traceable back to the single “best” satellite estimate. In the present implementation, the calibration is based on TRMM estimates. The TMPA is computed twice as part of the routine processing for TRMM, first as an experimental best-effort real-time monitoring product about 9 h after real time, and then as a post-real-time research-quality product about 10–15 days after the end of each month. (For brevity, these will be referred to as the RT and research products, respectively.) The first has been posted to the Web since February 2002, while the second is available from January 1998, for a record that totals more than 9 yr and continues to grow.

Throughout this paper the research product will be described first, then modifications for producing the RT product will be outlined. Section 2 describes the input datasets, while section 3 describes the algorithms and section 4 gives dataset status. Section 5 describes some tests of algorithm performance and gives some examples for applying the TMPA to typical applications. Section 6 presents concluding remarks.

## 2. Input datasets

Most of the coverage in the TMPA depends on input from two different sets of sensors. First, precipitation-related passive microwave data are collected by a variety of low earth orbit (LEO) satellites, including the Microwave Imager (TMI) on TRMM, Special Sensor Microwave Imager (SSM/I) on Defense Meteorological Satellite Program (DMSP) satellites, Advanced Microwave Scanning Radiometer–Earth Observing System (AMSR-E) on *Aqua*, and the Advanced Microwave Sounding Unit–B (AMSU-B) on the National Oceanic and Atmospheric Administration (NOAA) satellite series. These data have a strong physical relationship to the hydrometeors that result in surface precipitation, but each individual satellite provides a very sparse sampling of the time–space occurrence of precipitation. Even taken together, there are significant gaps in the

current 3-hourly coverage by the passive microwave estimates. The snapshot in Fig. 1 for a particular 3-hourly period is representative of current “full” microwave coverage, averaging about 80% of the earth’s surface in the latitude band  $50^\circ\text{N}$ – $50^\circ\text{S}$ . The complement of satellite-borne passive microwave sensors has shown steady improvement over the span of the TMPA data record (Fig. 2), starting with three satellites in 1998 that averaged about 40% coverage in each 3-h period.

In the current TMPA system, passive microwave fields of view (FOVs) from TMI, AMSR-E, and SSM/I are converted to precipitation estimates at the TRMM Science Data and Information System (TSDIS) with sensor-specific versions of the Goddard Profiling Algorithm (GPROF; Kummerow et al. 1996; Olson et al. 1999) for subsequent use in the TMPA. GPROF is a physically based algorithm that attempts to reconstruct the observed radiances for each FOV by selecting the “best” combination of thousands of numerical model-generated microwave channel upwelling radiances. The associated vertical profiles of hydrometeors then are used to provide an estimated surface precipitation rate. The microwave data are screened for contamination by surface effects as part of the processing, with marginal contamination denoted as “ambiguous.”

Passive microwave FOVs from AMSU-B are converted to precipitation estimates at the National Environmental Satellite, Data, and Information Service (NESDIS) with operational versions of the Zhao and Weng (2002) and Weng et al. (2003) algorithm. Ice water path (IWP) is computed from the 89- and 150-GHz channels, with a surface screening that employs ancillary data. Precipitation rate is then computed based on the IWP and precipitation rate relationships derived from cloud-model data computed with the fifth-generation Pennsylvania State University–National Center for Atmospheric Research (Penn State–NCAR) Mesoscale Model (MM5). The maximum precipitation rate allowed is  $30 \text{ mm h}^{-1}$ . The AMSU-B algorithm can discriminate between precipitating and nonprecipitating ice-bearing clouds but cannot provide information on precipitation systems that lack the ice phase. The multichannel conically scanning passive microwave sensors (TMI, AMSR-E, SSM/I) have a similar limitation over land, so the AMSU-B estimates are roughly comparable. However, over ocean the conical scanners also sense liquid hydrometeors, providing additional sensitivity, including to precipitation from clouds that lack the ice phase. As a result, the AMSU-B estimates over ocean are relatively less capable in detecting precipitation over ocean. The lack of the lightest rain occurs in all ocean areas, but it is most important in the subtropical highs, where all of the rain events are light. A sec-

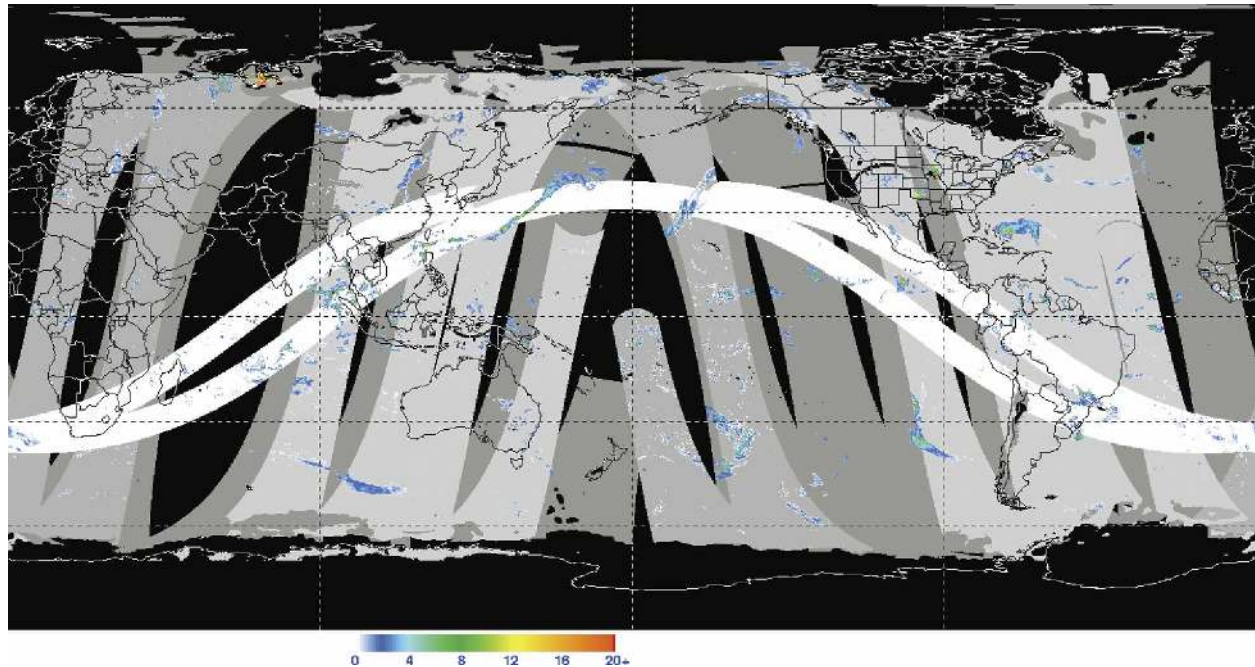


FIG. 1. Combined microwave precipitation estimate for the 3-h period centered at 0000 UTC 25 May 2004 in  $\text{mm h}^{-1}$ . Blacked-out areas denote regions that lack reliable estimates, while the zero values in the remaining areas are color-coded to depict the coverage by the various sensors. The order of precedence for display and corresponding zero color are TMI (white), SSM/I (light gray), AMSR-E (medium gray), and AMSU-B (dark gray). (In the TMPA the TMI, SSM/I, and AMSR-E are averaged where overlaps occur.)

ond issue in the current AMSU-B algorithm is that it neglects calibration differences across the swath due to variations in the size of individual FOVs. This variation introduces unphysical variability into the resulting AMSU-B estimates that must be corrected in a future release (Joyce and Ferraro 2006).

The second major data source for the TMPA is the window-channel ( $\sim 10.7 \mu\text{m}$ ) infrared (IR) data that are being collected by the international constellation of geosynchronous earth orbit (GEO) satellites. In contrast to the sparse temporal sampling of the passive microwave data, the GEO-IR data provide excellent time-space coverage. The CPC of the NOAA/National Weather Service (NWS) merges the international complement of GEO-IR data into half-hourly  $4 \text{ km} \times 4 \text{ km}$  equivalent latitude-longitude grids (hereafter the “CPC merged IR”; Janowiak et al. 2001). The IR brightness temperatures ( $T_b$ ) are corrected for zenith-angle viewing effects and intersatellite calibration differences.

For TMPA research estimates generated prior to the start of the CPC merged IR dataset in early 2000 (see Fig. 2), we use a GPCP dataset (also produced at CPC) that contains 24-class histograms of GEO-IR  $T_b$  data on a 3-hourly,  $1^\circ \times 1^\circ$  latitude-longitude grid covering the latitude band  $40^\circ\text{N}$ – $40^\circ\text{S}$  (hereafter the “GPCP IR histograms”; Huffman et al. 2001). This dataset also in-

cludes grid-box-average Geostationary Operational Environmental Satellite (GOES) Precipitation Index (GPI; Arkin and Meisner 1987) estimates computed from LEO-IR data recorded by the NOAA satellite series. These LEO-GPI data are used in the TMPA to fill gaps in the GEO-IR coverage, most notably in the Indian Ocean sector, where there was no GEO-IR coverage before *Meteorological Satellite 5* (*Meteosat-5*) began providing observations there in June 1998.

All IR-based precipitation estimates share the limitation that the  $T_b$ 's primarily correspond to cloud-top temperature, and implicitly cloud height. Arkin and Meisner (1987) showed that such information is poorly correlated to precipitation at fine time/space scales but is relatively well correlated at scales larger than about 1 day and  $2.5^\circ \times 2.5^\circ$  of latitude-longitude.

Finally, the research TMPA also makes use of three additional data sources: the TRMM Combined Instrument (TCI) estimate, which employs data from both TMI and the TRMM precipitation radar (PR) as a source of calibration (TRMM product 2B31; Haddad et al. 1997a,b); the GPCP monthly rain gauge analysis developed by the Global Precipitation Climatological Center (GPCC; Rudolf 1993); and the Climate Assessment and Monitoring System (CAMS) monthly rain gauge analysis developed by CPC (Xie and Arkin 1996).



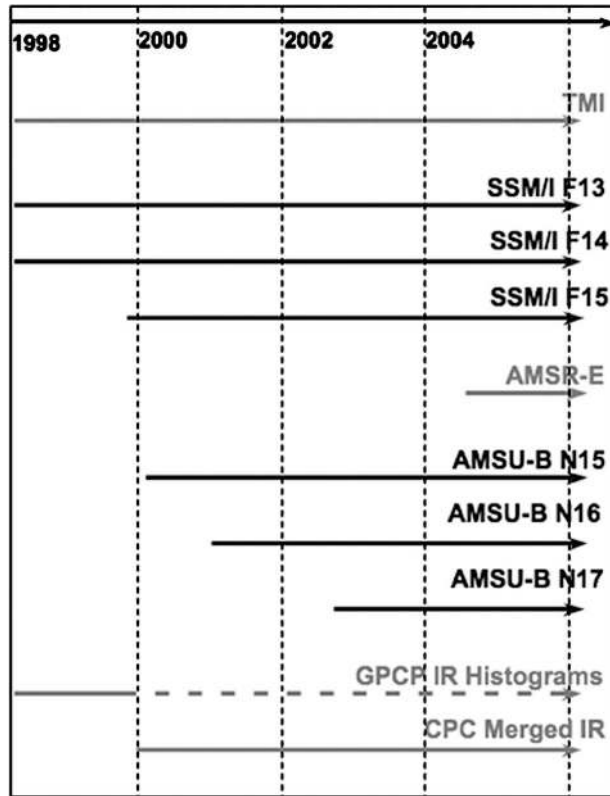


FIG. 2. Data availability during the TRMM era for satellite sensors used in the TMPA. Solid lines denote periods when the data are used in the (version 6) research product, and dashed indicates when they are available but not used.

During the early TMPA design work, the authors realized that they could obtain (restricted) access to the requisite microwave and IR data within a few hours of observation time. “Real time” (or more strictly, near-real time) production makes the estimates useful to several new classes of users. At the same time, experience indicated that bias adjustments based on monthly gauge data materially improve the accuracy of the estimates (Huffman et al. 1995, among others). These considerations led to the two-track approach of computing both RT and research products. In the following sections we describe the research product approach, then introduce the necessary changes that distinguish the RT algorithm.

### 3. TMPA algorithms

The TMPA estimates are produced in four stages: 1) the microwave precipitation estimates are calibrated and combined, 2) infrared precipitation estimates are created using the calibrated microwave precipitation, 3) the microwave and IR estimates are combined, and 4)

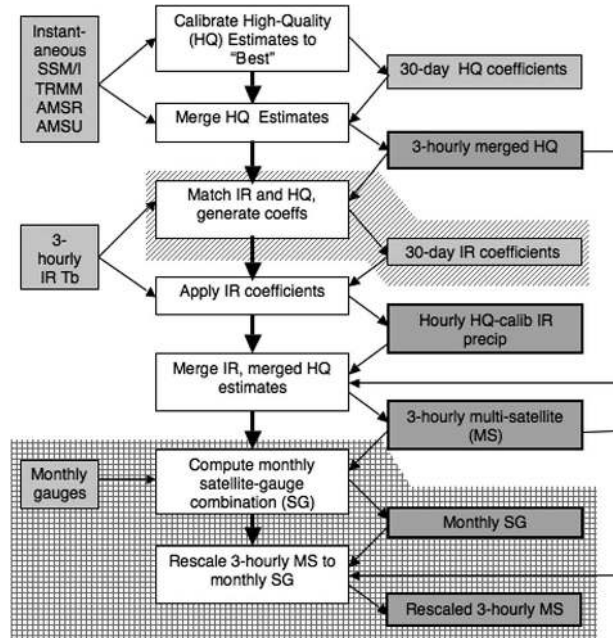


FIG. 3. Block diagram for both the RT and research product algorithms, showing input data (left side), processing (center), output data (right side), data flow (thin arrows), and processing control (thick arrows). The items on the slanted shading run asynchronously for the RT algorithm, and the items on the grid shading are only performed for the research product. “Best” in the top center shaded box is the TMI GPROF precipitation estimate for the RT algorithm and the TMI-PR combined algorithm precipitation estimate for the research product.

rain gauge data are incorporated. Figure 3 presents a block diagram of the TMPA estimation procedure. Each TMPA precipitation field is best interpreted as the precipitation rate effective at the nominal observation time.

#### a. Combined microwave estimates

All of the available passive microwave data are converted to precipitation estimates on individual FOVs, then each dataset is averaged to the  $0.25^\circ$  spatial grid over the time range  $\pm 90$  min from the nominal 3-hourly observation times (0000, 0300, ..., 2100 UTC). The gridding is “forward”—each FOV is averaged into the grid box that contains its center—except the AMSU-B gridding is “backward”—each FOV is approximately apportioned to the grid box(es) it occupies. All of these estimates are adjusted to a “best” estimate using probability matching of precipitation rate histograms assembled from coincident data, similar to the probability-matched method suggested by Miller (1972) and used, for example, by Krajewski and Smith (1991). The research product algorithm takes the TCI as the calibrating data source following the results of the prelimi-

nary validation of version-6 TRMM products. However, the coincidence of TCI with any of the sensors other than TMI is sparse, so we establish a TCI-TMI calibration, which is then applied to the TMI calibrations of the other sensors to estimate the TCI-calibrated values. The TCI-TMI relationship is computed on a  $1^\circ \times 1^\circ$  grid for each month using that month's coincident data aggregated on overlapping  $3^\circ \times 3^\circ$  windows to accommodate the somewhat different regional climatologies of the two estimates.

Preliminary work showed that the TMI calibrations of the other sensors' estimates are adequately represented by climatologically based coefficients representing large areas. In the case of the TMI-SSM/I calibration, separate calibrations are used for five oceanic latitude bands ( $40^\circ$ – $30^\circ$ N,  $30^\circ$ – $10^\circ$ N,  $10^\circ$ N– $10^\circ$ S,  $10^\circ$ – $30^\circ$ S,  $30^\circ$ – $40^\circ$ S) and a single land-area calibration for each of the four 3-month seasons. The TMI-AMSR-E and TMI-AMSU-B calibrations are set in the form of a single climatological adjustment for land and another for ocean. The AMSU-B calibration has two additional issues. First, the NESDIS algorithm changed on 31 July 2003, so separate sets of calibrations are provided for the two data periods. Second, in both periods the AMSU-B fractional occurrence of precipitation in the subtropical highs is notably deficient. After extensive preliminary testing, the authors judged it best to develop the ocean calibration in regions of significant precipitation and apply it everywhere, recognizing that the resulting fields would have a somewhat low bias. For all sensors the calibration is a simple matchup of histograms. For simplicity, in all cases the calibrations in the  $40^\circ$ – $50^\circ$  latitude belts in both hemispheres are taken to be the calibrations that apply just equatorward of  $40^\circ$ .

A calibration interval of a month is chosen to ensure stability and representativeness, except for the TMI-AMSR-E calibration, which requires 2 months for stability. The TCI-TMI calibration interval for the research product is a calendar month, and the resulting adjustments are applied to data for the same calendar month. This choice is intended to keep the dependent and independent datasets for the calibrations as close as possible in time.

How do the individual intercalibrated precipitation estimates compare? All sensor types except the AMSR-E recorded views of a storm southeast of Sri Lanka during the 3-h period centered on 0000 UTC 2 May 2004 (Fig. 4). The enlargement for each subfigure was done without interpolation so that individual grid-box values are relatively easy to identify. While each sensor depicts similar large-scale structure, considerable quantitative disagreement exists at the finescale. Differences in observation times certainly are one fac-

tor; the shifts in location of the main rain system just south of the equator are broadly consistent with its westward motion and the observation times for each of the sensors. The viewing angles of the LEO satellites differ widely for these particular overpasses, giving the possibility that each records a different radiometric mix from the same three-dimensional scenes. An additional issue for the AMSU-B is that its cross-track scanning smooths fields due to the enlargement of FOVs at the swath edge. Such differences have an important role in creating the large uncertainties at the finest scales, discussed below.

Once the input microwave estimates are calibrated for each satellite and grid boxes containing  $>40\%$  ambiguous FOVs are reset to "missing," the grid is populated by the "best" data from all available overpasses. When there are multiple overpasses in the 3-hourly window for a given grid box, data from TCI, TCI-adjusted TMI, TCI-adjusted AMSR-E, and TCI-adjusted SSM/I are averaged together. Tests show that the histogram of precipitation rate is somewhat sensitive to the number of overpasses averaged together, so in the future we plan to test a scheme taking the single "best" overpass in the data window period. In contrast, the TCI-adjusted AMSU-B estimates are used only if none of the others are available for the grid box, due to the detectability deficiency in the AMSU-B estimates over ocean discussed above. Figure 5 (top) provides an example combined microwave field. The data voids (gray areas) arise both from the lack of data during the 3-h period (outside the smoothly arcing swaths of data) and from unfavorable surface conditions (northern Japan and southern South America).

#### *b. Microwave-calibrated IR estimates*

As noted above, the research product uses two different IR datasets for creating the complete record of 3-hourly  $0.25^\circ$  gridded  $T_b$ 's. In the period from 1 January 1998 to 7 February 2000, each grid box's histogram in the  $1^\circ \times 1^\circ$  3-hourly GPCP IR histogram dataset is zenith-angle corrected, averaged to a single  $T_b$  value for the grid box, and plane-fit interpolated to the  $0.25^\circ$  grid. For the period from 7 February 2000 onward, the CPC merged IR is averaged to  $0.25^\circ$  resolution and combined into hourly files as  $\pm 30$  min from the nominal time. The amount of imagery delivered to CPC varies by satellite operator, but international agreements mandate that full coverage be provided at the 3-hourly synoptic times (0000, 0300, . . . , 2100 UTC). Histograms of time-space matched combined microwave [or high quality (HQ)] precipitation rates and IR  $T_b$ 's, each represented on the same  $3\text{-hourly } 0.25^\circ \times 0.25^\circ$  grid, are accumulated for a month into histograms on a  $1^\circ \times 1^\circ$

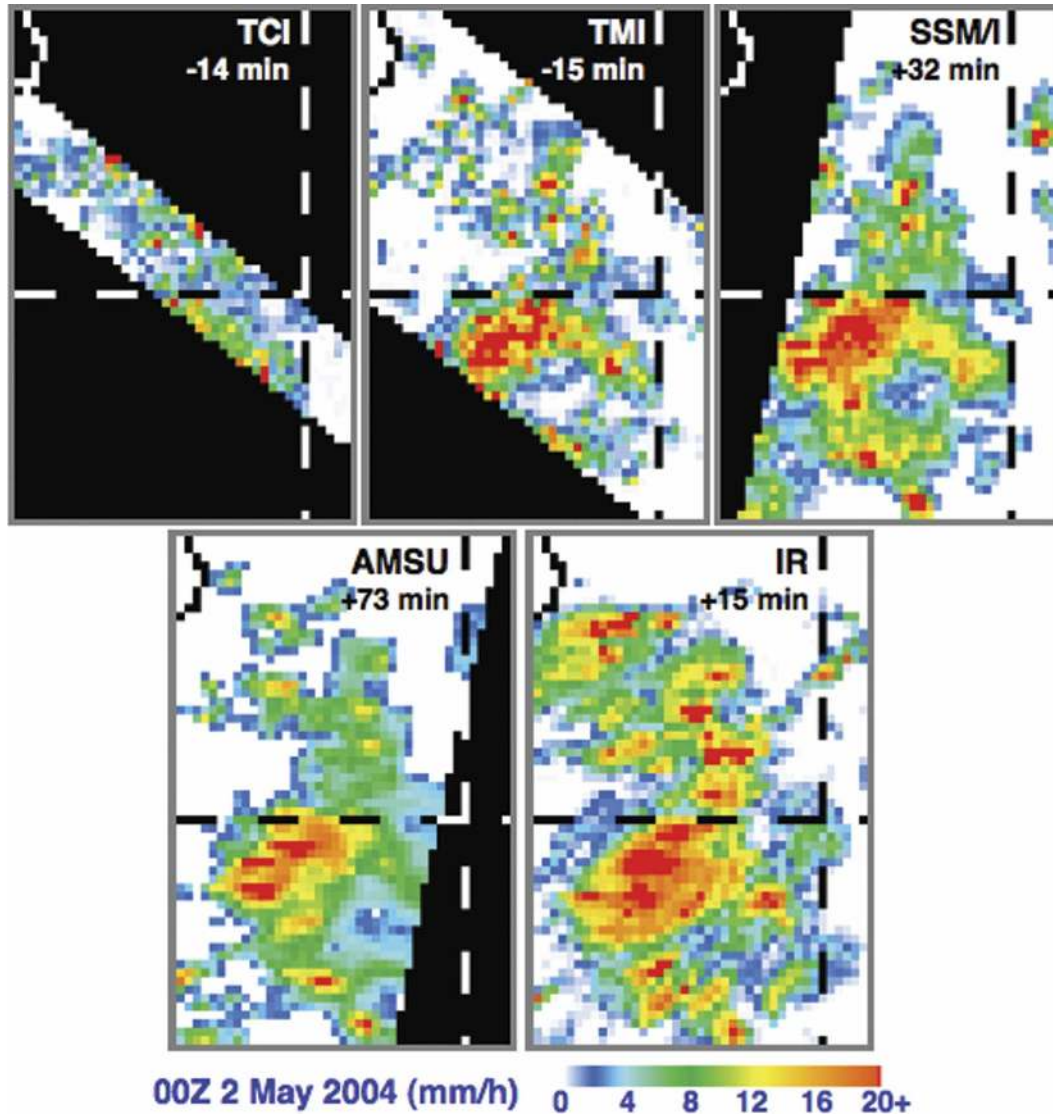


FIG. 4. Single-overpass snapshots from various intercalibrated satellite precipitation estimates for a region southeast of Sri Lanka for the 3-h period centered at 0000 UTC 2 May 2004. The SSM/I and AMSU-B swaths are from the DMSP *F13* and *NOAA-K* satellites, respectively. For each subimage, the southeastern coast of Sri Lanka is in the upper left corner, the equator is a horizontal dashed line, and longitude 90°E is a vertical dashed line. Black denotes missing data, except the latitude, longitude, and coast lines are white in data voids and black otherwise. The time offset of each image from the nominal 0000 UTC is given in minutes on each subimage.

grid, aggregated to overlapping  $3^\circ \times 3^\circ$  windows, and then used to create spatially varying calibration coefficients that convert IR  $T_b$ 's to precipitation rates. These coefficients approximately trace back to the TCI standard since the HQ inputs are all calibrated to the TCI. As in most of the calibrations for the HQ, the calibration month is the calendar month. Screening for ambiguous data described above for the HQ is also applied here to the coincident data to control artifacts.

By design, there is no precipitation when the  $0.25^\circ \times 0.25^\circ$  average  $T_b$  is greater than the local threshold

value, while increasingly colder  $T_b$ 's are assigned increasingly large precipitation rates using histogram matching. Those grid boxes that lack coincident data throughout the month, usually due to cold-land drop-outs or ambiguous editing, are given calibration coefficients by smooth-filling histograms of coincident data from surrounding grid boxes. Finally, preliminary testing showed that the precipitation rates assigned to the coldest  $T_b$ 's by strict probability matching tended to show unphysical fluctuations. To ameliorate this effect, a somewhat subjectively chosen coldest 0.17% of the  $T_b$



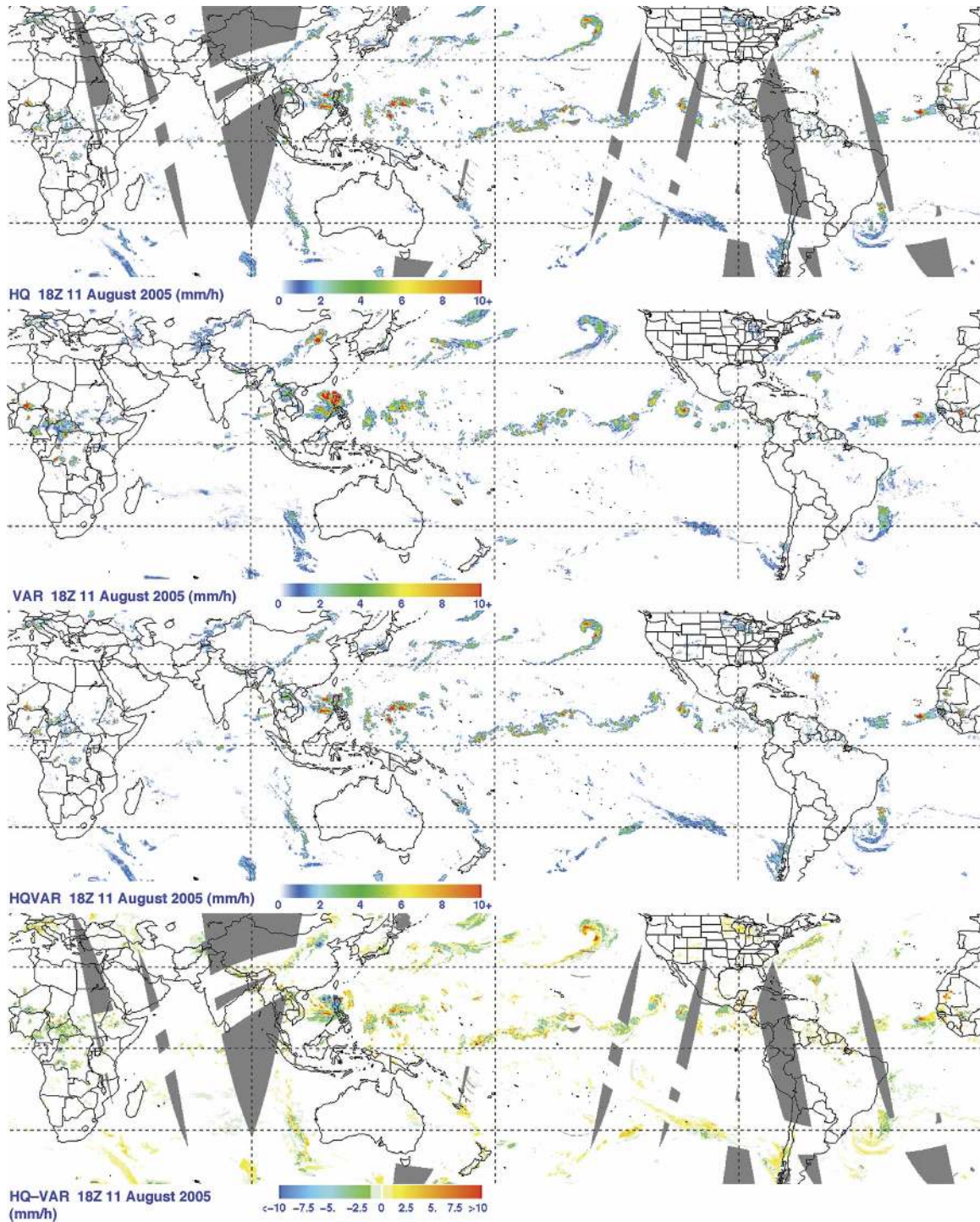


FIG. 5. Example of output from the RT algorithm, showing (top) the combined microwave field (HQ or 3B40RT), (upper middle) microwave-calibrated IR (VAR or 3B41RT), (lower middle) merged microwave IR field (HQVAR or 3B42RT), and (bottom) the HQ-VAR difference for the nominal observation time at 1800 UTC 24 Sep 2002. Grayed-out areas lack data for the calculation.

histogram is specified by a fourth-order polynomial fit to a climatology of coldest 0.17% precipitation rate points around the globe. In each grid box a constant is added to the climatological curve to make it piecewise

continuous with the grid box's  $T_b$ -precipitation rate curve at the 0.17%  $T_b$ .

Once computed, the HQ-IR calibration coefficients are applied to each 3-hourly IR dataset during the

month. Figure 5 (upper middle) provides an example microwave-calibrated field; spatial coverage by the IR is nearly complete in the latitude band for which we compute estimates (50°N–S). Note in Fig. 4 how the IR subfigure qualitatively agrees with the individual intercalibrated microwave estimates, although the area-average precipitation rate and coverage by precipitation happen to display higher values in that case.

### c. Merged microwave and IR estimates

The ultimate goal of this project is to provide the “best” estimate of precipitation in each grid box at each observation time. It is frequently quite challenging to combine different estimates of an intermittent field such as precipitation. The process of combining passive microwave estimates is relatively well behaved because the sensors are quite similar and GPROF is used for most retrievals. This is not the case for the microwave and IR fields, as shown in the difference field in Fig. 5 (bottom). In addition to the seemingly random differences that we would expect, there are also systematic differences (discussed below).

Given these issues, we apply a simple approach for combining the microwave and IR estimates, namely, the physically based combined microwave estimates are taken “as is” where available, and the remaining grid boxes are filled with microwave-calibrated IR estimates. This scheme provides the “best” local estimate, at the expense of a time series that contains heterogeneous statistics. Qualitatively, the example merged field in Fig. 5 (lower middle) displays few noticeable data boundaries, in part due to the strong spatial variability that real precipitation systems exhibit. Note the rain systems associated with then-Tropical Storm Irene (east of the Bahamas), and Hurricanes Fernando and Greg (southwest and south of Baja California, Mexico). A midlatitude low pressure center and trailing front are located north of Hawaii, and late-afternoon convection is decaying in central Africa.

The difference field (Fig. 5, bottom) facilitates a comparison of the two fields. The convective systems, such as the African thunderstorms and hurricanes, tend to show local differences, most likely due to the delay in time between the occurrence of precipitation and the growth of cirrus at the top of the storm. The midlatitude system shows a larger-scale offset, which is interpreted as resulting from the frontal-scale offset between high-level cirrus ahead of the system and the precipitation, which is located closer to the low pressure center and frontal zone. Some of the offsets shown in the difference field could also be due to the 3-h window for microwave data.

Images of the 3-hourly algorithm are best viewed as movie loops, examples of which are posted online at <http://trmm.gsfc.nasa.gov> under the button labeled “Realtime 3 Hourly & 7 Day Rainfall.”

### d. Rescaling to monthly data

The final step in the research product is the use of rain gauge data. It is highly advantageous to include rain gauge data in combination datasets (Huffman et al. 1997, among others). However, experience shows that on any time scale shorter than a month the gauge data are neither reported with sufficient density nor reported with consistent observational intervals to warrant direct inclusion in a global algorithm. The authors solved this issue in the GPCP One-Degree Daily combination dataset by scaling the short-period estimates to sum to a monthly estimate that includes monthly gauge data (Huffman et al. 2001). Here, we take a similar approach: all available 3-hourly merged estimates are summed over a calendar month to create a monthly multisatellite (MS) product. The MS and gauge are combined as in Huffman et al. (1997) to create a post-real-time monthly SG combination, which is a TRMM research-grade product in its own right (3B43). Then the field of SG/MS ratios is computed on the  $0.25^\circ \times 0.25^\circ$  grid (with controls) and applied to scale each 3-hourly field in the month, producing the version-6 3B42 product. This gauge adjustment step is denoted in Fig. 3 with grid shading. The result is to provide the high resolution typical of satellite data and the typically small bias of gauge analyses over land.

### e. RT algorithm adjustments

The RT and research product systems are designed to be as similar as possible to ensure consistency between the resulting datasets. The first important difference is that the calibrator used for the research product, the TCI, is not available in real time. In its absence we use the TMI estimates from TRMM. In the future we plan to test the PR as the standard for calibration in both the research and RT products.

Second, a real-time system cannot reach into the future, so the calibration month is taken as a trailing accumulation of 6 pentads.<sup>1</sup> Before February 2005, the TMI–SSM/I intercalibration and the microwave–IR coefficients are each recomputed at the end of each pentad, while thereafter the intercalibration of individual

<sup>1</sup> A pentad is a 5-day period, except when Leap Day is included in the pentad that encompasses it. There are 73 pentads in each year, starting with 1–5 January.



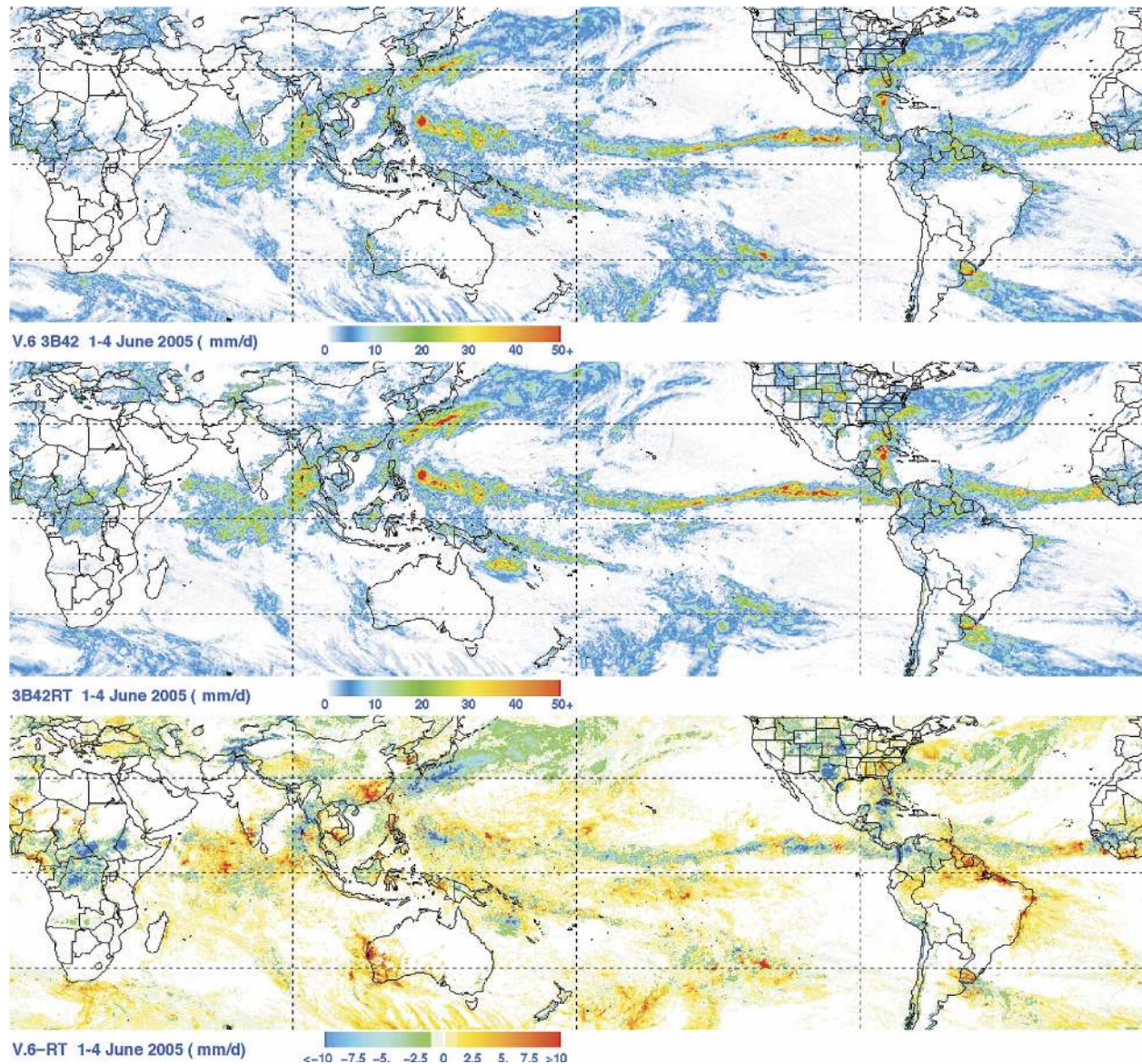


FIG. 6. Example accumulations of (top) research (version-6 3B42) and (middle) RT (3B42RT) products, and (bottom) the map of differences for the period 1–4 Jun 2005 in  $\text{mm day}^{-1}$ .

microwave estimates to the TMI is handled with climatological coefficients, and the microwave-IR calibrations are recomputed at each 3-hourly time from the five trailing and one current (partial) pentad. The slant shading in Fig. 3 denotes the calibration steps in the algorithm block diagram. The change in microwave intercalibration was made for computational simplicity and in preparation for possible loss of TRMM data. The change in microwave-IR calibration was intended to better capture rapid changes in the calibration for rare heavy rain events, as discussed in section 5c.

A third important difference for the RT system is that the monthly gauge adjustment step carried out for

the research product is not possible. We plan to develop a climatological adjustment to minimize the biases between the RT and research products due to both differences in calibration source and in use of gauge data.

Figure 6 typifies the relation between the RT and research products. Each data source is averaged over the 4-day period 1–4 June 2005, arbitrarily chosen from the epoch with the “current” RT algorithm and intended to give a sort of synoptic-scale picture. Large-scale averages of the two fields are within a few percent of each other, but systematic regional differences are apparent. For the most part, these should reflect the

differences in the calibrations applied to the two datasets. The ITCZ is somewhat lower amplitude and broader in the (TCI calibrated) research product, compared to the (TMI calibrated) RT. In the southern extratropics the research product is higher almost everywhere, while the picture is decidedly mixed in the northern extratropics. Over land the TCI calibration is importantly modified by the indirect use of the rain gauge analysis in creating the final version-6 3B42. Low values in interior tropical Africa, central Asia, and the Great Plains in the United States, as well as higher values in equatorial Amazonia and along the southwestern coast of India are consistent with known issues with microwave-based estimates in those regions.

#### 4. Dataset status

The RT system has been running routinely on a best-effort basis in TSDIS since late January 2002 and is currently on its third release. For simplicity, a fixed 9-h latency is used as the trigger to run the processing, a delay that typically captures >95% of potential microwave estimates. The combined microwave, microwave-calibrated IR, and merged microwave-IR estimates, which are labeled 3B40RT, 3B41RT, and 3B42RT, respectively, are available from <ftp://trmmopen.gsfc.nasa.gov> or <http://precip.gsfc.nasa.gov>. The research product system has been developed as the version-6 algorithm for the TRMM operational product 3B42, although that product only provides the final gauge-adjusted merged field. The version-6 TRMM 3B43 product has been developed as the post-real-time monthly SG precipitation product described above. Version-6 data are available for January 1998 to the (delayed) present at <http://disc.sci.gsfc.nasa.gov/data/datapool/TRMM/>, and an interactive analysis and display capability is provided at <http://disc2.nascom.nasa.gov/Giovanni/tovas>.

#### 5. Comparisons and examples

Various studies examining the performance and utility of early versions of the RT product have already appeared. For example, Katsanos et al. (2004) examined daily scale performance against gauge data in the eastern Mediterranean Sea and found that the TMPA-RT performed best when precipitation was relatively frequent but suffered a bias at high rain rates. In this section we provide a few representative comparisons of TMPA performance and show some typical uses. More comprehensive evaluations are in preparation as part of the long-term intercomparison of quasi-operational global precipitation datasets over continental-scale re-

gions, the Program for Evaluation of High-Resolution Precipitation Products (PEHRPP), being organized by the International Precipitation Working Group (IPWG) of the Coordinating Group for Meteorological Satellites (Turk et al. 2006).

##### a. Comparison data

###### 1) KWAJALEIN ISLAND, RMI RADAR

The TRMM Ground Validation (GV) group collects operational radar scans from the radar at Kwajalein Island (KWAJ), Republic of the Marshall Islands (RMI), to which they apply the recently developed relative calibration adjustment (RCA) to correct ongoing uncertainty with the radar's calibration (Marks et al. 2005; Silberstein et al. 2005). The recalibrated reflectivities are quality controlled, then matched against coincident rain gauge data using the Window Probability Matching Method (WPMM; Rosenfeld et al. 1994) to generate Ze-R relationships that vary over time and range from the radar. The resulting TRMM 2A-53 GV product is a 2 km  $\times$  2 km instantaneous rain map every half hour extending 150 km from KWAJ (Wolff et al. 2005). For this study, the 2-km data were averaged to the 0.5° grid used for comparison to the buoy gauges and accumulated to 3-hourly and monthly intervals. Residual artifacts, periods of data unavailability, and small-scale fluctuations in the Ze-R relationship all introduce uncertainty into the results.

###### 2) NWS MELBOURNE, FLORIDA, WEATHER SURVEILLANCE RADAR-1988 DOPPLER (WSR-88D)

Similarly, the TRMM GV group collects operational radar scans from the NWS radar at Melbourne, Florida (MELB), quality controls them, then applies WPMM to generate the MELB TRMM 2A-53 GV product. No RCA is needed at MELB.

###### 3) AUSTRALIAN GAUGE DATA

Daily precipitation analyses over Australia are provided by the Bureau of Meteorology, where reports from up to 6000 gauges are quality controlled and objectively analyzed to a 0.25°  $\times$  0.25° latitude-longitude grid (Weymouth et al. 1999). The quality of the analysis depends on the density of gauge reports (sparser data imply larger errors), the complexity of the local terrain (since gauges in mountain areas are generally sited in valleys and, therefore, underreport the true areal average rainfall), and undercatch. The undercatch is primarily due to aerodynamic effects at the mouth of the gauge (Sevruk 1989), but we usually lack the requisite



data to compute the time-dependent correction for each station. The Legates (1987) climatological corrections seem to indicate that the bias should be less than 10% in many tropical and warm-season temperate areas.

#### 4) ATOLL GAUGE DATA

The Comprehensive Pacific Rainfall Database (PACRAIN; Morrissey and Greene 1991) provides daily and/or monthly island-sited rain gauge data from the western and central tropical Pacific Ocean. The present study follows the common practice of selecting stations sited on atolls and treating them as representative of the open ocean in their region, although this approximation continues to generate controversy. Possible errors include misidentification of missing values as zeroes and undercatch.

#### 5) BUOY GAUGE DATA

Multiyear observations of rainfall are being recorded on selected buoys in the Triangle Trans Ocean Buoy Network (TRITON) and Tropical Atmosphere Ocean (TAO) programs in the west and east Pacific Ocean, respectively (McPhaden et al. 1998). In the present study the original 10-min rain rates (Serra et al. 2001) are averaged over 3-h intervals centered on the synoptic observing times, and then all rates below  $0.1 \text{ mm h}^{-1}$  are set to zero. This thresholding is necessary to control the noise that broadens the spike in the rain-rate histogram at zero rain rate into a Gaussian centered slightly below zero; the threshold value was chosen in a preliminary examination of the rain-rate histogram for several buoy gauges with significant rain. As with the other gauge data sources, the major source of error is likely a negative bias due to undercatch.

#### 6) NERN

An integral part of the North American Monsoon Experiment (NAME), which is focused on northwestern Mexico, is an array of 87 tipping-bucket gauges that are arranged in transects from sea level to the heights of the Sierra Madre known as the NAME Event Rain Gauge Network (NERN; Gochis et al. 2004). The array is specifically laid out to capture the strong orographic influence on precipitation that is known to dominate the region's climatology.

### b. Comparisons

#### 1) MONTHLY

Ebert (2005) presented one early set of monthly results that uses the Australian rain gauge datasets intro-

duced above. In general, she finds that the various satellite estimates, including early versions of the TMPA-RT, perform best in relatively heavy, convective, warm-season regimes, while they perform more poorly in relatively light, cool-season regimes that are more midlatitude in nature. The version of 3B42RT operational in 2004 showed a definite seasonal cycle, with Australia-average positive (negative) monthly bias during the warm (cool) season and correlation coefficients hovering around 0.50 (0.30) in the warm (cool) season. In contrast, we find that the version-6 3B42 results are significantly closer to the validation data, as one might expect with implicit gauge calibration. Correlation coefficients exceed 0.90 for 10 of the 12 months in 2004 and there is no obvious seasonal cycle in the bias. Meanwhile, 3B42RT showed a mean absolute monthly bias of roughly 28% for the entire year 2004, while the version-6 TMPA mean absolute monthly bias for 2004 only approaches 9%. The bias over all of Australia for 2004 is 6.8%, which is interpreted as mostly reflecting the climatological undercatch correction that we apply to the TMPA, but which is not present in the Australian analysis. Ebert et al. (2007) present further comparisons for Australia, the United States, and the United Kingdom that reproduce and extend the results quoted here.

Turning to the oceans, the atoll and buoy rain gauge datasets introduced above may be used as the surface reference data because they are not included in processing 3B42/43. The finest possible spatial scale for these comparisons is  $0.5^\circ \times 0.5^\circ$  latitude-longitude because the buoys are all located at the corners of the  $0.25^\circ$  grid boxes. Figure 7 provides the scatterplot for all monthly matchups of (single) rain gauge and averaged version-6 3B43, which is essentially the monthly sum of 3B42. The atoll scattergram (Fig. 7a) is quite consistent with the buoy scattergram (Fig. 7b), showing nearly equitable scatter about the 1:1 line with roughly linear bias over the range of rain rates. Table 1 lists the corresponding basic statistics of average, bias, and root-mean-square (RMS) difference. The consistency between the atoll and buoy results tends to build confidence that these two rather different data sources are in fact giving a realistic assessment. Further analysis will investigate climate regime dependence, an effect that is illustrated by separating the buoy data into locations west and east of the date line (Fig. 7b; Table 1).

In contrast to the point estimates produced by gauges, the radar estimates from KWAJ are true area averages for a tropical ocean area. The 6-yr monthly plot in Fig. 7c shows all the  $0.5^\circ$  grid-box comparisons within the 100-km range limit for KWAJ, so it only represents one area, while the gauge plots cover vast



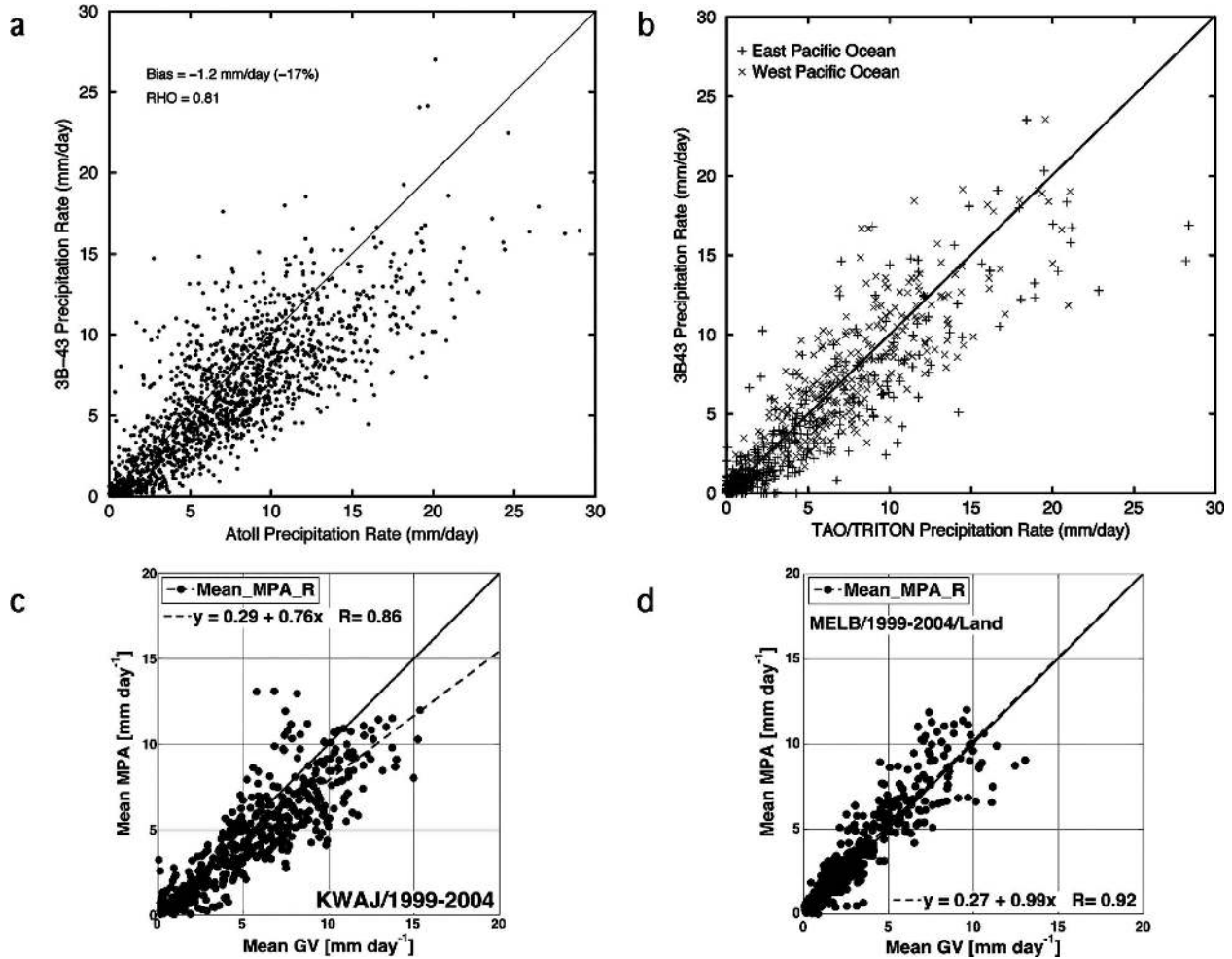


FIG. 7. Scattergrams comparing monthly research product (version-6 3B42) precipitation estimates to monthly averages reported by single gauges located on (a) atolls and (b) TAO/TRITON buoys for the 7-yr period January 1998 to December 2004, as well as to (c) Kwajalein radar and (d) overland Melbourne radar estimates for the 6-yr period January 1999 to December 2004. All gridding is at  $0.5^\circ \times 0.5^\circ$  monthly, values are expressed as  $\text{mm day}^{-1}$ , and the buoy reports are separated into west and east Pacific (west and east of the date line, shown as x's and + 's, respectively).

reaches of the tropical Pacific. Nonetheless, the general patterns within the scatterplots are similar. The statistics in Table 1 reinforce the conclusion that the radar and gauge results are consistent at the monthly scale.

Recalling that none of the gauge data have been corrected for undercatch, we note that the bias against the atoll gauges is close to that against the KWAJ radar estimates, which are calibrated by similar island-based

TABLE 1. Average, bias, and RMS difference statistics comparing monthly accumulations reported at single gauges located on atolls and TAO/TRITON buoys, and monthly  $0.5^\circ \times 0.5^\circ$  accumulations of calibrated radar estimates with collocated monthly  $0.5^\circ \times 0.5^\circ$  accumulations of the monthly research product (version-6 3B43) for the 7-yr period January 1998 to December 2004. All values are expressed as  $\text{mm day}^{-1}$  or percentages, as appropriate.

Gauge source	No. of comparisons	Avg observed precipitation	Bias (3B43 – obs)	RMS difference
Atolls	1572	7.27	−1.21 (−16.6%)	3.10 (42.4%)
All buoys	1021	3.87	−0.29 (−7.5%)	1.95 (50.4%)
West Pacific buoys	323	7.26	−0.16 (−2.2%)	2.34 (32.2%)
East Pacific buoys	698	2.32	−0.35 (−15.2%)	1.74 (75.0%)
KWAJ	504	5.40	−0.99 (−18.4%)	1.94 (36.0%)
MELB land	441	3.26	+0.23 (+7.1%)	1.17 (35.4%)

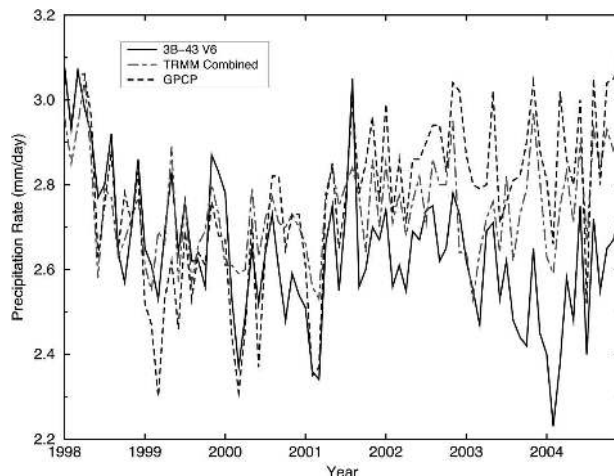


FIG. 8. Time series of the monthly research product (version-6 3B43; solid), version-6 TRMM Combined Instrument 3B31 (gray dash-dot), and GPCP version-2 SG (dashed) averaged over ocean regions in the latitude band  $30^{\circ}\text{N}$ – $\text{S}$ .

gauges sited around Kwajalein Atoll. On the other hand, the bias against the buoy gauges is noticeably smaller. We suspect that this is largely due to larger undercatch by the buoy gauges. A definitive study of undercatch by the buoy gauges is lacking, but Serra et al. (2001) give a range of estimates that is greater than is typical for land-based gauges, in part because the buoy gauges are mounted relatively high above the surface and in part because the wide-open ocean sites present fewer obstacles to the wind than most land sites. This discussion makes it clear that a better evaluation is needed for undercatch by the buoy gauges.

As a comparison using consistent analysis methods, we analyze overland matchups to the Melbourne WSR-88D (Fig. 7d; Table 1). Although the patterns are similar, the Melbourne land results show a smaller bias and less scatter across the range of rain rates. We attribute these improvements to the gauge adjustment that the research product incorporates over land.

Taking an even larger-scale view, consider the monthly time series of precipitation averaged over ocean regions for the latitude band  $30^{\circ}\text{N}$ – $\text{S}$  (Fig. 8). The version-6 3B43 (again, essentially the sum of the month's 3B42; shown as a solid line) is closely related to the TCI (gray dash-dot line) that is taken as the calibration standard for the passive microwave input fields, except that over time the 3B43 shifts to a negative bias of almost 10%. This result stems from the AMSU-B rain estimates currently in use. First, as discussed earlier, the current AMSU-B algorithm fails to detect light rain over oceans, particularly in the subtropical highs. We tempered the influence of this AMSU-B deficiency by only using AMSU-B when no other microwave types

were available, but it is impossible to rescale the AMSU-B rain values that are zero. So, the successive introduction of AMSU-B satellites during 2000–02 leads to an increasingly negative bias. A second issue for the AMSU-B is that a revised algorithm was applied to data observed after 30 July 2003, and the revised algorithm has additional difficulty in identifying light precipitation over ocean, even though the overall nature of the rain retrieved is better. The authors and the algorithm developers are presently working to develop a correction approach for the AMSU-B algorithm. A comparable issue usually does not arise over land because all of the microwave estimates are limited to scattering algorithms, erasing the advantage that the conical scan sensors have over ocean, and because the rain gauge calibration step keeps the monthly TMPA close to the “right” answer.

The GPCP version 2 is also included on Fig. 8 for comparison (dashed line), and it tracks rather closely with the TCI and version-6 3B43, except for the drift in 3B43 bias that we ascribe to AMSU-B. The calibrator for GPCP over ocean is the Chang–Chiu–Wilheit emission algorithm computed for a single-SSM/I time series (Adler et al. 2003), which is quite different than the TCI. This agreement helps build confidence in each result.

## 2) DAILY/SUBDAILY

Moving to shorter time scales, the TMPA estimates show considerably more uncertainty, in common with other short-interval precipitation estimates and for the reasons illustrated by Fig. 4. It is a challenging area of current research to adequately characterize and resolve these uncertainties. In this section we focus on illustrating some representative behavior of the TMPA at fine scales. Figure 9 gives a representative time series of the 3-hourly version-6 3B42 averaged over a  $0.5^{\circ}$  box centered at  $5^{\circ}\text{N}$ ,  $165^{\circ}\text{E}$  (in the western Pacific ITCZ) for May 2004, as well as the 3-hourly TAO/TRITON buoy accumulations at that location. Despite the differences in sampling, the two agree on the occurrence of most precipitation events. Note that each precipitation event lasts for only a small number of 3-h periods, typical of the convective nature of the ITCZ. The cumulative distributions in this particular case are relatively close throughout the month; in other cases a different sequence of over- and underestimates might lead the cumulative distribution to be systematically low or high for most of the month, even though the month might well end in relatively close agreement. Any of these outcomes is consistent with the design goal of the TMPA, which is that the histogram of 3-hourly estimates approximates the histogram of rain that a good

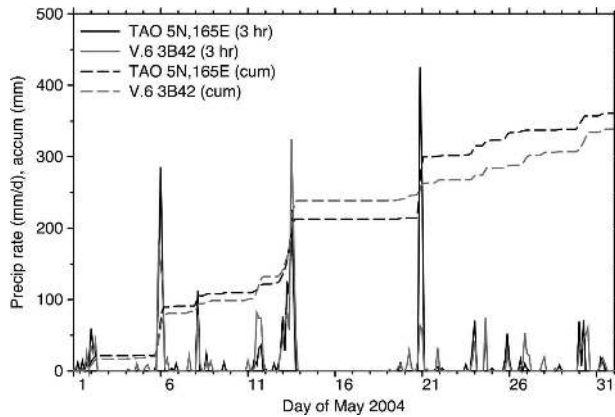


FIG. 9. Time series of the 3-hourly precipitation from the gauge on the TAO/TRITON buoy at  $5^{\circ}\text{N}$ ,  $165^{\circ}\text{E}$  (black) and the surrounding  $0.5^{\circ} \times 0.5^{\circ}$  average of the research product (version-6 3B42; gray) for May 2004. The 3-hourly data are shown with solid lines ( $\text{mm day}^{-1}$ ) and the corresponding cumulative time series are shown with dashed lines (mm).

validation array would observe over the same area and time period.

Success at this design goal is demonstrated in the matched data histograms of precipitation at the  $0.5^{\circ} \times 0.5^{\circ}$  3-hourly scale from KWAJ for all of 2001 (Fig. 10). The graphs are representative of other years of data as well. The important high-end tail matches rather closely, while the TMPA estimates show a somewhat more peaked distribution at middle and low values than the radar. This results both from the native histogram in

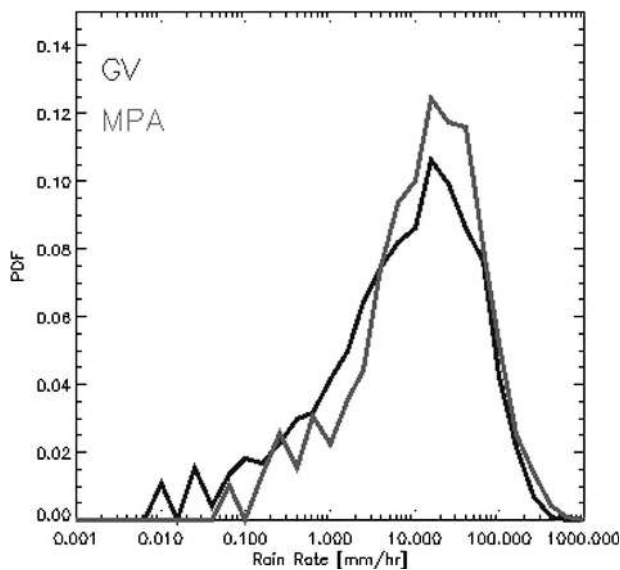


FIG. 10. Histograms comparing 3-h  $0.5^{\circ} \times 0.5^{\circ}$  precipitation rates reported by the Kwajalein radar (black) with collocated precipitation estimates from the research product (version-6 3B42; gray) for 2001.

the Kwajalein region of the calibration source, the TCI, and from the detectability problems noted above in the various satellite estimates, particularly from AMSU-B.

The scattergram for all daily  $0.5^{\circ} \times 0.5^{\circ}$  matchups between the buoy gauges and version-6 3B42 estimates for the 7-yr period January 1998 to December 2004 is shown in Fig. 11. Compared to the monthly plots in Fig. 7 there is much more scatter, as is typical of such short-interval estimates, particularly when continuous accumulations at a single point (gauge) are scattered against sums of area-average snapshots (satellite). For daily rain rates less than about  $20 \text{ mm day}^{-1}$  the distribution of points is approximately constant along lines perpendicular to the 1:1 line, while at higher rain rates the points cluster toward the 1:1 line. It is typical of noisy, calibrated estimates that the days with high rates emerge as showing skill first, while the lower values (the majority of days) tend to be less skillful as a group. Throughout, the distribution is approximately symmetric about the 1:1 line, although close inspection reveals that more points lie to its right in agreement with the monthly bias results.

### c. Examples

Among the wide range of possible uses for TMPA estimates, monitoring for extreme precipitation events has high societal impact (Negri et al. 2005). In late May

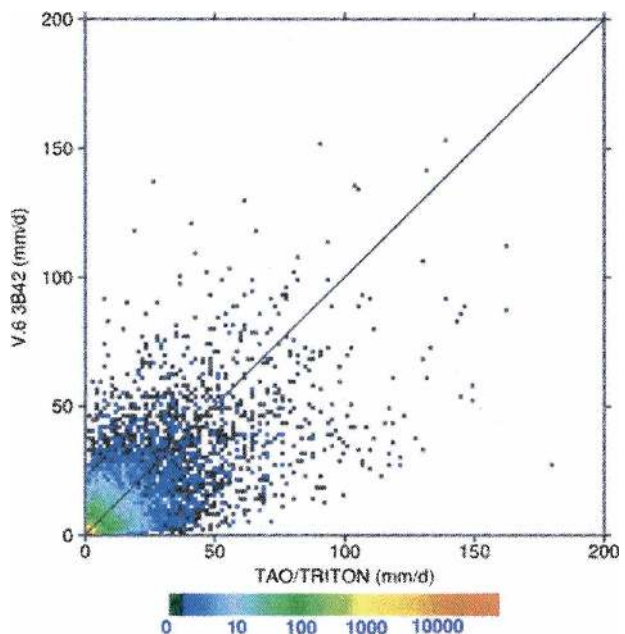


FIG. 11. Scattergrams comparing daily accumulations reported at single gauges located on TAO/TRITON buoys with collocated daily  $0.5^{\circ} \times 0.5^{\circ}$  accumulations of the research product (version-6 3B42) precipitation estimates for the 7-yr period January 1998 to December 2004. All values are expressed as  $\text{mm day}^{-1}$ .



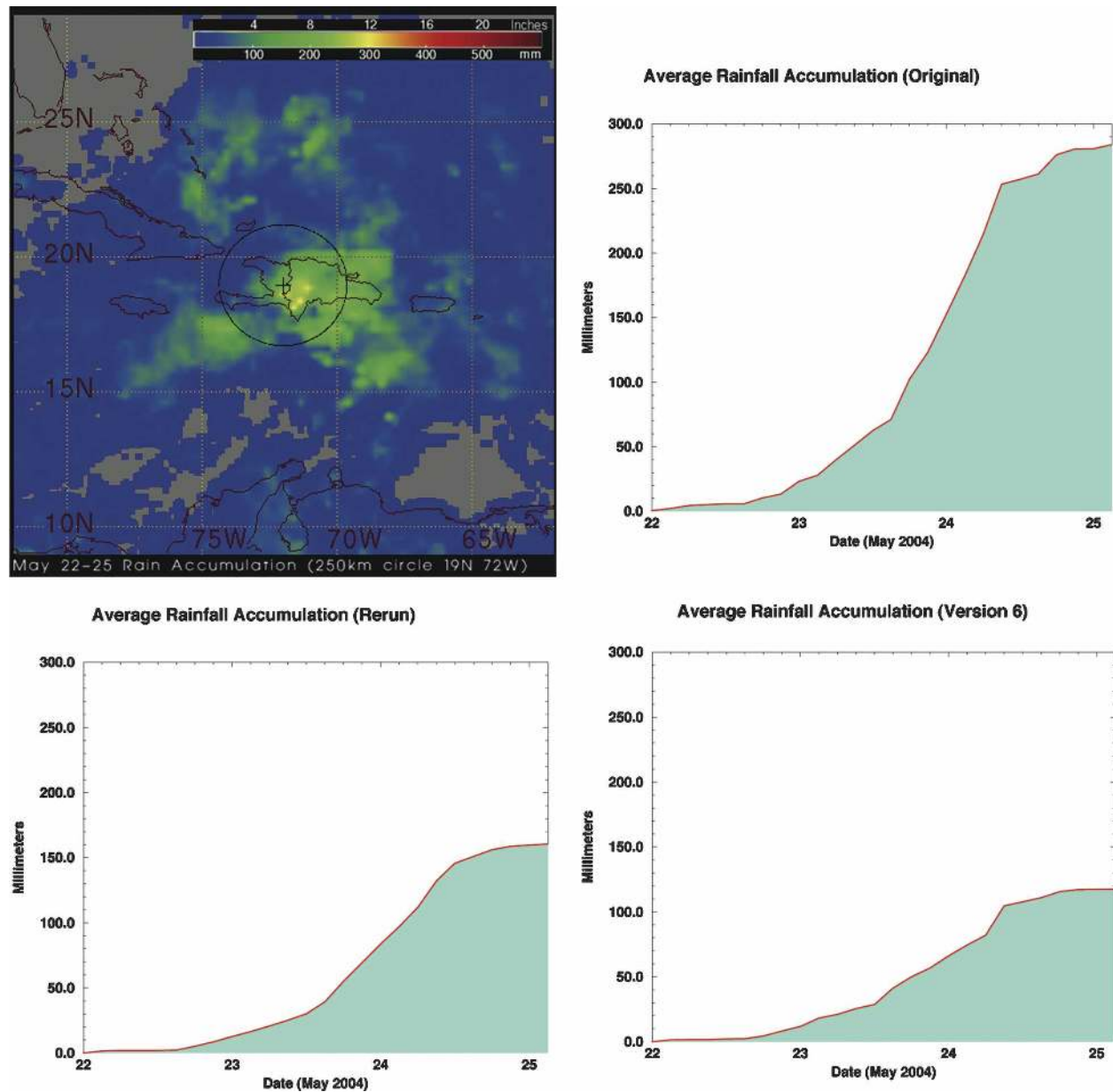


FIG. 12. (top left) Accumulation map and time series of accumulation averaged within the 250-km range ring centered at 19°N, 72°W over the period 22–24 May 2004 for (top right) the original RT (3B42RT), (bottom left) a recalibrated RT, and (bottom right) the research product (version-6 3B42). The range ring is depicted on the map as the black circle roughly centered on Hispaniola.

2004 an area of disturbed weather moved from south to north across the island of Hispaniola, causing torrential rains, flash flooding, and upward of 2000 fatalities. This system failed to qualify even as a tropical depression but required a significant international relief response. In real time, the then-operational 3B42RT estimates showed a highly concentrated event in the south-central part of the island (Fig. 12, upper left) primarily occurring on 24 May (Fig. 12, upper right). Postanalysis seemed to suggest that the estimates were high, and at

that time the RT scheme only computed a new IR calibration every 5 days, meaning the IR estimates, which formed the bulk of the data, were only calibrated by pre-event microwave data. When we shifted the IR calibration month later by a single 5-day period to include the flood event, the recalibrated high-end IR estimates were lower by a factor of almost 2 (Fig. 12, lower left). This result indicated that extreme events were more sensitive to the calibration than we had expected, and it led us to shift the RT system to recalibrating the IR

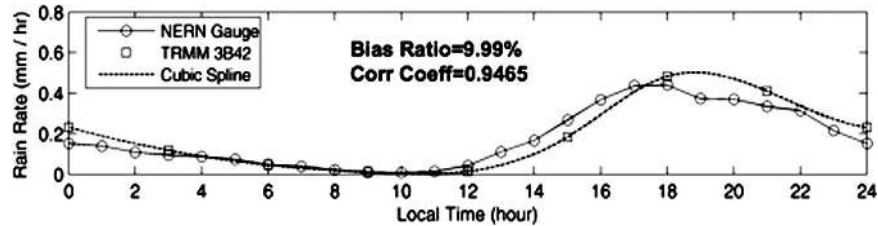


FIG. 13. Comparison of diurnal cycle for the research product (version-6 3B42; squares) and NERN (dots) for the 2004 summer season (June–August). A cubic-spline interpolation between research product estimates is shown as a dashed line.

coefficients every 3 h. Nonetheless, even this new, lower value is symptomatic of a dangerous flood-inducing event. When the version-6 3B42 was computed (Fig. 12, lower right), it was similar to the revised RT (Fig. 12, lower left), although the research product featured a stronger burst around 1000 UTC 24 May. Since the research product features both a calibration period that encompasses the flood event and much more microwave data than the then-operational 3B42RT, it appears that the IR calibration was the dominant source of uncertainty in the RT analysis.

Another important application of short-interval precipitation estimates such as the TMPA is to estimate the diurnal cycle of precipitation. Such information is important for validating model performance, as well as providing decision makers with background data on the most likely times for heavy rain events. Comparing the version-6 3B42 to the NERN in northwestern Mexico for the 2004 summer season (June–August; Fig. 13), the overall shape of the estimated diurnal cycle has good agreement with observations. The main difference is that the diurnal maximum through the afternoon and evening is shifted somewhat more than 1 h later in the TMPA and is somewhat stronger at its peak. This delay warrants further investigation because the plentiful microwave estimates that dominate the research product at this time are generally considered closely related to coincident surface precipitation.

## 6. Concluding remarks

The TMPA has been developed to take advantage of the increasingly rich constellation of satellite-borne precipitation-related sensors. Estimates are provided at relatively fine scales ( $0.25^\circ \times 0.25^\circ$ , 3 hourly) in both post-real and real time to facilitate use by a wide range of researchers. However, the errors inherent in the finest scale estimates are large. The most successful use of the TMPA data is to take advantage of the fine scales to create averages appropriate to the user's application.

Looking to future work, the first task for the authors

is to further characterize the performance of this approach and explore differences between the RT and research products. As part of this effort, we plan to participate in PEHRPP (Turk et al. 2006). We also plan to explore climatological adjustments to the RT product to minimize its biases against the research version. Another important effort is to improve intercalibration of the microwave-based estimates, particularly addressing the oceanic light-precipitation deficiencies in the current AMSU-B input.

At the same time, we expect to start extending the estimates to the poles by incorporating fully global precipitation estimates based on Television Infrared Observation Satellite (TIROS) Operational Vertical Sounder (TOVS), Advanced TOVS (ATOVS), and Advanced Infrared Sounder (AIRS) data. The best approach to combining the microwave and IR estimates is also a topic for future research. It would be helpful to develop a better IR-based algorithm so that the combination would not have to reconcile the strong fine-scale differences that currently exist between the two. We will consider shortening the production interval to, say, hourly to better resolve the diurnal cycle and will consider shifting the definition of the observation times to better align with validation data. Finally, the study of precipitation in general needs a succinct statistical description of how errors in finescale precipitation estimates should be aggregated through scales up to global/monthly.

On the instrumentation side there is a concerted effort to provide complete 3-hourly microwave data. Most of this effort is focused on the National Aeronautics and Space Administration's Global Precipitation Measurement (GPM) project. GPM is working to increase the frequency of coverage by encouraging the launch of additional precipitation-related sensors, and to provide a next-generation TRMM-like "core" satellite to calibrate all of the passive microwave estimates on an ongoing basis. We expect the GEO-IR-based estimates to have a long-term role in filling the inevitable gaps in microwave coverage, as well as in enabling

sub-3-hourly precipitation estimates at fine spatial scales.

**Acknowledgments.** The authors thank Mr. Harold Pierce for creating Fig. 12, and Mr. Robert Joyce and an anonymous reviewer for constructive suggestions that improved the paper.

#### REFERENCES

- Adler, R. F., and Coauthors, 2003: The Version-2 Global Precipitation Climatology Project (GPCP) Monthly Precipitation Analysis (1979–present). *J. Hydrometeorol.*, **4**, 1147–1167.
- Arkin, P. A., and B. N. Meisner, 1987: The relationship between large-scale convective rainfall and cold cloud over the Western Hemisphere during 1982–84. *Mon. Wea. Rev.*, **115**, 51–74.
- Ebert, E. E., 2005: Satellite vs. model rainfall—Which one to use? *Fifth Int. Scientific Conf. on the Global Energy and Water Cycle*, Orange County, CA, Global Energy and Water Experiment. [Available online at [http://www.gewex.org/5thConfposterT6-7\\_Ebert.pdf](http://www.gewex.org/5thConfposterT6-7_Ebert.pdf).]
- , J. E. Janowiak, and C. Kidd, 2007: Comparison of near-real-time precipitation estimates from satellite observations and numerical models. *Bull. Amer. Meteor. Soc.*, in press.
- Gochis, D. J., A. Jimenez, C. J. Watts, W. J. Shuttleworth, and J. Garatuza-Payan, 2004: Analysis of 2002 and 2003 warm-season precipitation from the North American Monsoon Experiment Event Rain Gauge Network. *Mon. Wea. Rev.*, **132**, 2938–2953.
- Haddad, Z. S., D. A. Short, S. L. Durden, E. Im, S. Hensley, M. B. Grable, and R. A. Black, 1997a: A new parameterization of the rain drop size distribution. *IEEE Trans. Geosci. Remote Sens.*, **35**, 532–539.
- , E. A. Smith, C. D. Kummerow, T. Iguchi, M. R. Farrar, S. L. Durden, M. Alves, and W. S. Olson, 1997b: The TRMM “day-1” radar/radiometer combined rain-profiling algorithm. *J. Meteor. Soc. Japan*, **75**, 799–809.
- Huffman, G. J., 2005: Satellite-based estimation of precipitation using microwave sensors. *Encyclopedia of Hydrological Sciences*, M. G. Anderson, Ed., John Wiley and Sons, 965–980.
- , R. F. Adler, B. Rudolf, U. Schneider, and P. R. Keehn, 1995: Global precipitation estimates based on a technique for combining satellite-based estimates, rain gauge analysis, and NWP model precipitation information. *J. Climate*, **8**, 1284–1295.
- , and Coauthors, 1997: The Global Precipitation Climatology Project (GPCP) combined precipitation dataset. *Bull. Amer. Meteor. Soc.*, **78**, 5–20.
- , R. F. Adler, M. Morrissey, D. T. Bolvin, S. Curtis, R. Joyce, B. McGavock, and J. Susskind, 2001: Global precipitation at one-degree daily resolution from multisatellite observations. *J. Hydrometeorol.*, **2**, 36–50.
- Janowiak, J. E., R. J. Joyce, and Y. Yarosh, 2001: A real-time global half-hourly pixel-resolution infrared dataset and its applications. *Bull. Amer. Meteor. Soc.*, **82**, 205–217.
- Joyce, R. J., and R. R. Ferraro, 2006: Improvements of CMORPH resulting from limb adjustments and normalization of AMSU-B rainfall. Preprints, *14th Conf. on Satellite Meteorology and Oceanography*, Atlanta, GA, Amer. Meteor. Soc., CD-ROM, P1.22.
- , J. E. Janowiak, P. A. Arkin, and P. Xie, 2004: CMORPH: A method that produces global precipitation estimates from passive microwave and infrared data at high spatial and temporal resolution. *J. Hydrometeorol.*, **5**, 487–503.
- Katsanos, D., K. Lagouvardos, V. Kotroni, and G. J. Huffman, 2004: Statistical evaluation of MPA-RT high-resolution precipitation estimates from satellite platforms over the central and eastern Mediterranean. *Geophys. Res. Lett.*, **31**, L06116, doi:10.1029/2003GL019142.
- Kidd, C. K., D. R. Kniveton, M. C. Todd, and T. J. Bellerby, 2003: Satellite rainfall estimation using combined passive microwave and infrared algorithms. *J. Hydrometeorol.*, **4**, 1088–1104.
- Krajewski, W. F., and J. A. Smith, 1991: On the estimation of climatological Z–R relationships. *J. Appl. Meteor.*, **30**, 1436–1445.
- Kummerow, C., W. S. Olson, and L. Giglio, 1996: A simplified scheme for obtaining precipitation and vertical hydrometeor profiles from passive microwave sensors. *IEEE Trans. Geosci. Remote Sens.*, **34**, 1213–1232.
- Legates, D. R., 1987: *Climatology of Global Precipitation*. Publications in Climatology, Vol. 40, University of Delaware, 85 pp.
- Marks, D. A., D. B. Wolff, D. S. Silberstein, J. L. Pippitt, and J. Wang, 2005: Improving radar rainfall estimates at Kwajalein Atoll, RMI through relative calibration adjustments. Preprints, *32d Conf. on Radar Meteorology*, Albuquerque, NM, Amer. Meteor. Soc., CD-ROM, 3R.2.
- McPhaden, M. J., and Coauthors, 1998: The tropical ocean global atmosphere (TOGA) observing system: A decade of progress. *J. Geophys. Res.*, **103**, 14 169–14 240.
- Miller, J. R., 1972: A climatological Z–R relationship for convective storms in the northern Great Plains. Preprints, *15th Conf. on Radar Meteorology*, Champaign–Urbana, IL, Amer. Meteor. Soc., 153–154.
- Morrissey, M. L., and J. S. Greene, 1991: The Pacific atoll rain gauge dataset. Tech. Rep., Planetary Geosciences Division Contribution 648, University of Hawaii, 45 pp.
- Negri, A. J., and Coauthors, 2005: The Hurricane–Flood–Landslide Continuum. *Bull. Amer. Meteor. Soc.*, **86**, 1241–1247.
- Olson, W. S., C. D. Kummerow, Y. Hong, and W.-K. Tao, 1999: Atmospheric latent heating distributions in the Tropics derived from satellite passive microwave radiometer measurements. *J. Appl. Meteor.*, **38**, 633–664.
- Rosenfeld, D., D. B. Wolff, and E. Amitai, 1994: The window probability matching method for rainfall measurements with radar. *J. Appl. Meteor.*, **33**, 682–693.
- Rudolf, B., 1993: Management and analysis of precipitation data on a routine basis. *Proceedings of International Symposium on Precipitation and Evaporation*, Vol. 1, B. Sevruck and M. Lapin, Eds., Slovak Hydrometeorology Institution, 69–76.
- Serra, Y. L., P. A’Hearn, P. Freitag, and M. J. McPhaden, 2001: ATLAS self-siphoning rain gauge error estimates. *J. Atmos. Oceanic Technol.*, **18**, 1980–2001.
- Sevruck, B., 1989: Reliability of precipitation measurements. *Proc. WMO/LAHS/ETH Workshop on Precipitation Measurements*, St. Moritz, Switzerland, World Meteorological Organization, 13–19.
- Silberstein, D. S., D. B. Wolff, D. A. Marks, and J. L. Pippitt, 2005: Using ground clutter to adjust relative radar calibration at Kwajalein, RMI. Preprints, *32d Conf. on Radar Meteorol-*



- ogy, Albuquerque, NM, Amer. Meteor. Soc., CD-ROM, 3R.1.
- Sorooshian, S., K.-L. Hsu, X. Gao, H. V. Gupta, B. Imam, and D. Braithwaite, 2000: Evaluation of PERSIANN system satellite-based estimates of tropical rainfall. *Bull. Amer. Meteor. Soc.*, **81**, 2035–2046.
- Turk, F. J., and S. D. Miller, 2005: Toward improving estimates of remotely sensed precipitation with MODIS/AMSR-E blended data techniques. *IEEE Trans. Geosci. Remote Sens.*, **43**, 1059–1069.
- , P. Bauer, E. Ebert, and P. A. Arkin, 2006: Satellite-derived precipitation verification activities within the International Precipitation Working Group (IPWG). Preprints, *14th Conf. on Satellite Meteorology and Oceanography*, Atlanta, GA, Amer. Meteor. Soc., CD-ROM, P2.15.
- Weng, F., L. Zhao, R. Ferraro, G. Poe, X. Li, and N. Grody, 2003: Advanced microwave sounding unit cloud and precipitation algorithms. *Radio Sci.*, **38**, 8068–8079.
- Weymouth, G., G. A. Mills, D. Jones, E. E. Ebert, and M. J. Manton, 1999: A continental-scale daily rainfall analysis system. *Aust. Meteor. Mag.*, **48**, 169–179.
- Wolff, D. B., D. A. Marks, E. Amitai, D. S. Silberstein, B. L. Fisher, A. Tokay, J. Wang, and J. L. Pippitt, 2005: Ground validation for the Tropical Rainfall Measuring Mission (TRMM). *J. Atmos. Oceanic Technol.*, **22**, 365–380.
- Xie, P., and P. A. Arkin, 1996: Gauge-based monthly analysis of global land precipitation from 1971 to 1994. *J. Geophys. Res.*, **101**, 19 023–19 034.
- , J. E. Janowiak, P. A. Arkin, R. F. Adler, A. Gruber, R. Ferraro, G. J. Huffman, and S. Curtis, 2003: GPCP pentad precipitation analyses: An experimental dataset based on gauge observations and satellite estimates. *J. Climate*, **16**, 2197–2214.
- Zhao, L., and F. Weng, 2002: Retrieval of ice cloud parameters using the Advanced Microwave Sounding Unit. *J. Appl. Meteor.*, **41**, 384–395.

Copyright of Journal of Hydrometeorology is the property of American Meteorological Society and its content may not be copied or emailed to multiple sites or posted to a listserv without the copyright holder's express written permission. However, users may print, download, or email articles for individual use.